#### **Research Article**

Tongqing Li, Gary Chi-Pong Tsui\*, Chi-Ho Wong, Chak-Yin Tang, Kai Tang, and Youhua Tan

## Stimulus-responsive gradient hydrogel microactuators fabricated by two-photon polymerization-based 4D printing

https://doi.org/10.1515/ntrev-2025-0145 received September 17, 2024; accepted February 12, 2025

Abstract: The growing field of 4D printing has spurred extensive exploration into applications of stimulus-responsive materials, such as hydrogels for micro-actuators. However, the hydrogel-based micro-actuators fabricated by one-step, singlematerial printing are typically bilayer, and their actuation capabilities are limited. This study proposes a novel gradient printing strategy via two-photon polymerization (2PP) based 4D printing to enhance the actuation performance of stimulusresponsive hydrogel micro-actuators. The feasibility of this approach was demonstrated by investigating the shrinkage rates and elastic moduli of the poly(N-isopropylacrylamide) (PNIPAm) hydrogel micro-cuboids printed at different laser doses using the confocal laser scanning microscope and atomic force microscopy based nano-indentation respectively. The 2PP-based gradient printing was used to fabricate bilayer and trilayer PNIPAm hydrogel micro-actuators, with the laser dose programmed to modulate the crosslinking degree of each layer. These micro-actuators were actuated by near-infrared (NIR) light in the gold nanorods (AuNRs) solutions. The effects of the NIR light powers, micro-actuator sizes, and layer thicknesses on the actuation behaviors were systematically investigated. Compared with 12-µm-thickness bilayer micro-actuation, the introduction of the transitional layer into the gradient trilayer one significantly enhanced the actuation amplitude and speed (the bending angle and curvature increased by about 150 and 70%, respectively, and the cycle time of actuation and recovery shortened by 35%). These advancements have significant implications for printing microscale gradient materials and enhancing their applications.

**Keywords:** 4D printing, stimulus-responsive hydrogels, gradient printing, two-photon polymerization

## 1 Introduction

Micro-actuators, which can convert external stimuli into mechanical motion or deformation, show promise for diverse applications such as micro-robotics, biomedical devices, and soft microelectronics [1]. However, it is still challenging to fabricate soft micro-actuators with defined 3D structures and high actuation performance. 4D printing, an evolution of 3D printing, incorporates the temporal dimension and enables materials to morph, self-assemble, or respond to external stimuli over time [2,3]. 4D printing at the microscale allows the fabrication of dynamic microstructures with controllable functionalities [4], offering significant implications across disciplines such as biomedicine [5,6] and robotics [7]. The 4D-printed micro-actuators, with intricate motion and high actuation performance, can be fabricated by high-precision 4D printing technologies, such as two-photon polymerization (2PP) [8]. This precision 4D printing technology advances the development of intricate devices with tailored functionalities, particularly beneficial in microrobots [9], microfluidics [10], and electronics [11-13].

Compared to other soft materials used in the 4D printing of micro-actuators, such as shape memory

e-mail: mfgary@polyu.edu.hk, tel: +852 3400 3254, fax: +852 2362 5267 **Tongqing Li:** Advanced Manufacturing Technology Research Centre, Department of Industrial and Systems Engineering, The Hong Kong Polytechnic University, Hong Kong, China; State Key Laboratory of Ultraprecision Machining Technology, Department of Industrial and Systems Engineering, The Hong Kong Polytechnic University, Hung Hom, Kowloon, Hong Kong, China

**Chi-Ho Wong:** Division of Science, Engineering and Health Studies, School of Professional Education and Executive Development, The Hong Kong Polytechnic University, Hong Kong, China

**Chak-Yin Tang:** Advanced Manufacturing Technology Research Centre, Department of Industrial and Systems Engineering, The Hong Kong Polytechnic University, Hong Kong, China

**Kai Tang**, **Youhua Tan:** Department of Biomedical Engineering, The Hong Kong Polytechnic University, Hong Kong, China

<sup>\*</sup> Corresponding author: Gary Chi-Pong Tsui, Advanced Manufacturing Technology Research Centre, Department of Industrial and Systems Engineering, The Hong Kong Polytechnic University, Hong Kong, China; State Key Laboratory of Ultra-precision Machining Technology, Department of Industrial and Systems Engineering, The Hong Kong Polytechnic University, Hung Hom, Kowloon, Hong Kong, China,

polymers and liquid crystal elastomers, hydrogels have gained considerable attention and have been widely applied for sensors [14], drug delivery [15], biomedical [16], and soft robots [17-19] due to their unique biocompatible and tunable properties. These 3D crosslinked polymer networks, swollen with water, exhibit high biocompatibility, flexibility, and responsiveness to environmental changes [20,21]. Stimulus-responsive hydrogels, in particular, can undergo significant reversible changes in volume, shape, or mechanical properties in response to stimuli such as pH [22], temperature [23], light [24], electricity [25], and magnetic field [26]. Among the stimulus-responsive hydrogels, the poly (N-isopropylacrylamide) (PNIPAm) hydrogel is inherently temperature-responsive, and it can undergo a phase transition near its lower critical solution temperature (LCST) which is close to the physiological temperature. This phase transition enables the PNIPAm hydrogel to expand or contract when the temperature changes around its LCST, making it well suitable for applications requiring reversible and repeatable actuation. Moreover, it can incorporate photothermal materials, such as gold nanorods (AuNRs), to fabricate lightresponsive hydrogels. This light-driven hydrogel can be stimulated by light stimuli in a contactless manner by converting light into localized heat [25], unlike other types of stimulus-responsive hydrogels that require precise and complex stimulus control. These unique properties make the PNIPAm hydrogel become the suitable material for actuators [27]. By harnessing the responsiveness of hydrogels and 4D printing, the actuators can be engineered to perform intricate motion and shape transformations, mimicking biological systems. The tunable responsiveness and biocompatibility of hydrogel actuators further expand their utility in biomedical devices and soft robotics [28,29].

Various macroscale hydrogel actuators have been fabricated by 4D printing technologies such as direct ink writing (DIW) and stereolithography (SLA). However, at the microscale, the fabrication of hydrogel actuators presents several challenges, particularly in achieving precise and facile fabrication and enhanced actuation performance [30,31]. Current strategies, such as multi-material and multi-step printing, aim at printing heterogeneous-structured hydrogels [32,33]. For instance, bilayer soft micro-actuators made of PNIPAm and commercial IP-L were printed using the multi-material strategy [34]. This method encounters issues like complex fabrication processes and poor interfacial adhesion, resulting in interfacial delamination during actuation in bilayer actuators [35-37]. To address the interfacial problems, researchers have explored adding an intermediate layer to fabricate trilayer actuators [38,39]. For instance, the inclusion of a poly(2-ethylhexyl acrylate) interfacial layer between polyacrylamide and polyethylene

terephthalate layers has been proven to improve the actuation performance of the trilayer actuator [39]. Similarly, gradient structures exhibit transitional material properties across the heterogeneous structure and can alleviate interfacial adhesion problems [40,41]. Since the trilayer and gradient structure has been demonstrated to enhance the actuation performance of macro-actuators, the strategy of fabricating gradient trilayer structure would be a promising method for the actuation enhancement of micro-actuators. To fabricate such gradient trilayer micro-hydrogels, among the current 3D printing technologies such as DIW, SLA, and 2PP, 2PP technology has a high printing resolution (about 100 nm) beyond the diffraction limit achieved by focusing an ultrashort femtosecond laser pulse into a voxel of photosensitive material to initiate polymerization through two-photon absorption. It also allows programming the laser doses to fabricate heterogeneous microstructures in a single-material and one-step printing manner [42-44]. The laser dose can be tuned via 2PP-based printing through variations of the scanning speed and laser power [45] or the slicing and hatching distances to fabricate heterogeneous-structured bilaver micro-actuators [46]. The laser dose variation produces a difference in the crosslinking densities of hydrogel, thus causing a difference in swelling or shrinking capabilities for microactuator layers. Therefore, 2PP was used to fabricate gradient trilayer micro-actuators to improve the actuation performance and simplify the fabrication process. By leveraging the 2PP-based gradient printing strategy and trilayer microstructure, it is easy to print hydrogel micro-actuators with enhanced actuation performance.

In this article, we present a facile approach to fabricating stimulus-responsive hydrogel micro-actuators utilizing 2PP-based gradient printing (Figure 1). The gradient printing strategy was developed to achieve precise spatial control of the laser dose, enabling the fabrication of intricate structures with tailored material properties. Leveraging this strategy, the gradient bilayer-structured and multilayer-structured hydrogel stripes with varying sizes were designed. The crosslinking variations within the bilayer and gradient multilayer stripes were achieved by programming the laser dose. A series of gradient PNIPAm hydrogel micro-actuators were printed by a 780-nm femtosecond laser and subsequently actuated by 808-nm near-infrared (NIR) light in the AuNRs solutions. To the best of our knowledge, printing gradient micro-structures remains a challenge and has not been applied in the 4D printing of hydrogel microactuators. This research aims to fabricate gradient hydrogel micro-actuators with improved actuation performance using stimulus-responsive materials and a gradient printing strategy. The gradient-printed trilayer hydrogel micro-actuators demonstrated enhancement in the light-actuated

performance, including both bending amplitude and speed. This printing method highlights its versatility and potential applications in fabricating diverse materials and gradient microstructures.

## 2 Materials and methods

#### 2.1 Materials

N,N'-methylenebisacrylamide (MBA, 98%), 3-(trimethoxysilyl)propyl acrylate (TMSPA, 92%), and lithium phenyl (2,4,6-trimethylbenzoyl) phosphinate (LAP, 95%) were purchased from Sigma-Aldrich. Acrylic acid (AAc, 99.5%) was obtained from Thermo Scientific Chemicals, while methacryloxyethyl thiocarbamoyl rhodamine B was procured from Polysciences, Inc. Ethylene glycol (>99%), acetone (99.5%), isopropanol (>99.5%), *n*-hexane (ACS), ethanol (>99.8%) and chloroform (>99.8%) were purchased from Anagua Company Limited, Hong Kong. Poly(ethylene glycol) methyl ether thiol (mPEG-SH, Mn ≈ 2000) was procured from Sigma-Aldrich. All chemicals were used as received without additional purification or treatment. N-isopropylacrylamide (NIPAm, 97%) was purchased from Sigma-Aldrich, recrystallized in hexane, and stored at 4°C. Gold nanorods (AuNRs) (0.1 mg/mL, aspect ratio = 4:1) stabilized by cetyltrimethylammonium bromide (CTAB) were acquired from Xianfeng, China.

## 2.2 Preparation of photoresist and modification of AuNRs

The PNIPAm hydrogel photoresist was prepared by dissolving N-isopropylacrylamide (45 wt%), MBA (4 wt%), AAc (0.5 wt%), and LAP (1 wt%) with ethylene glycol (48 wt%). Methacryloxyethyl thiocarbamoyl rhodamine B (0.5 wt%) was also added for fluorescence imaging. The mixture was filtrated by 0.22 µm syringe filters. The as-prepared photoresist was put in a brown reagent bottle, stored at room temperature, and shielded from visible light to prevent undesired polymerization.

To obtain PEG-modified AuNRs, the CTAB-stabilized AuNRs were modified by HS-PEG-OCH3 according to the previously reported article [47]. The details of the procedures are presented in Supplementary Materials.

## 2.3 Design and fabrication of hydrogel micro-actuators

### 2.3.1 Design of 3D structures for the hydrogel microactuators

To demonstrate the effectiveness of gradient printing in enhancing actuation performance, the hydrogel microactuators were designed as bilayer and trilayer hydrogel stripes, utilizing the temperature-responsive property of

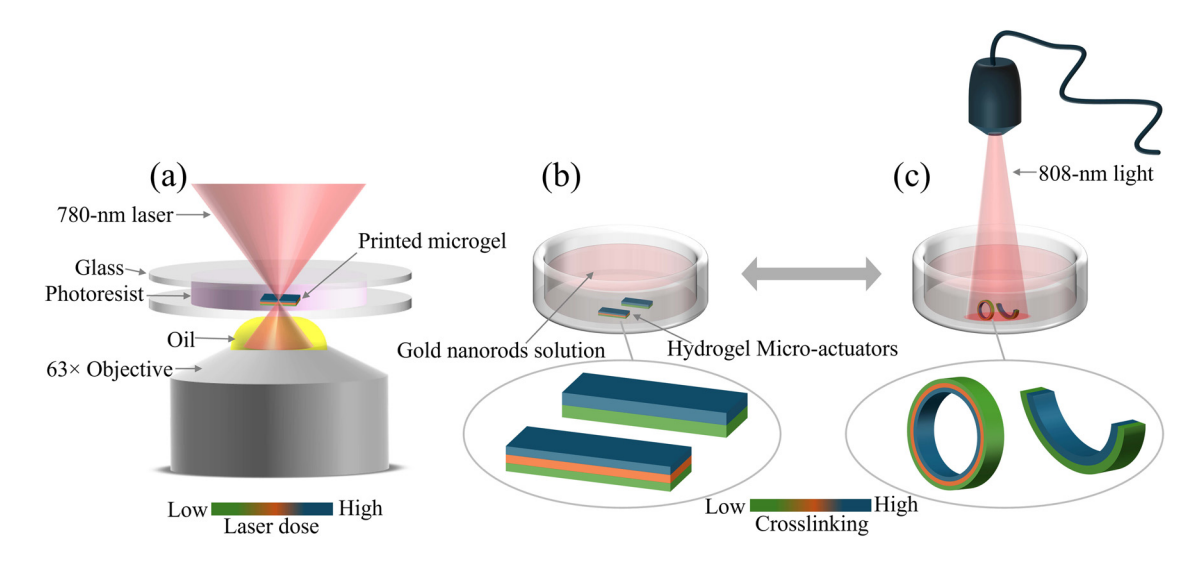


Figure 1: Schematic of fabrication and light-actuation of hydrogel micro-actuators. (a) Schematic of fabrication of hydrogel micro-actuators by 2PP using gradient printing; (b) gradient hydrogel micro-actuators immersed in the AuNR solution; and (c) 808-nm NIR light-actuation of gradient hydrogel micro-actuators.

the PNIPAm hydrogel [48], and the one-step, single-material gradient printing strategy. To achieve complex deformations like bending, the gradient printing strategy was employed to print heterogenous-structured PNIPAm hydrogel as the homogenous-structured PNIPAm hydrogel exhibits isotropic expansion or contraction. The gradient printing enables the fabrication of micro-actuators with gradient crosslinking across layers, driving the micro-actuators to bend [49]. The gradient crosslinking of the layers can be controlled by the gradient laser dose, which can be modulated by printing parameters such as laser power and scanning speed using the 2PP technology. Layers exposed to higher laser doses exhibit higher crosslinking, reduced shrinkage rates, and greater stiffness, while lower laser doses produce the opposite effect. However, excessive crosslinking can restrict deformation due to the low shrinkage rate and high rigidity. Additional design factors, including layer thickness and length, can influence the actuation speed and amplitude. By tailoring printing parameters, such as laser dose modulation, and structural factors, such as size and layer arrangement, the actuation performance of bilayer and trilayer micro-actuators can be systematically improved.

The gradient bilayer hydrogel micro-actuator was designed as a strip with upper and lower layers having different cross-linking densities (Figure 1). In contrast, the gradient trilayer hydrogel micro-actuator has a thinner layer thickness, and the laser dose variation between adjacent layers is less apparent than that of the bilayer ones. To study the effect of varying thicknesses and structures of the micro-actuators on their actuation performance, five microactuators with varying sizes and layer thicknesses were designed and labeled as micro-actuators a, b, c, d, and e (Table 1). The micro-actuators a, b, and d have gradient bilayer structures, while micro-actuators c and e possess gradient trilayer structures. The micro-actuator a has a length of 150 μm, while the others are 225 μm in length, with all micro-actuators having the same width. The thicknesses of micro-actuators a, b, and c are 12  $\mu$ m, whereas the micro-actuators d and e are 6  $\mu$ m thick. Based on the overall thickness and number of layers, the layer thicknesses of the micro-actuators a, b, c, d, and e were 6, 6, 4, 3, and  $2 \mu m$ , respectively.

**Table 1:** The size information of micro-actuators a-e

Name of micro-actuators	а	b	с	d	e
Length (µm)	150	225	225	225	225
Width (µm)	20	20	20	20	20
Thickness (µm)	12	12	12	6	6
Layer thickness (µm)	6	6	4	3	2

#### 2.3.2 Fabrication of hydrogel micro-actuators

The 3D structures of hydrogel micro-actuators with both bilayer and tri-layer structures were designed using SolidWorks 2016, and the resulting STL files were processed with Describe software to generate GWL files compatible with the Nanoscribe system. The 3D printing of the PNIPAm hydrogel micro-structures was conducted using a Photonic Professional DLW system (Nanoscribe GmbH, Germany). The printing was under the oil immersion mode using a 63× objective lens (numerical aperture of 1.4, Zeiss, Germany). A femtosecond laser with an emission wavelength of 780 nm served as the laser source. The pulse width and repetition rate were 120 fs and 100 MHz, respectively. The photoresist was exposed to the laser beam according to CAD design, resulting in polymerization and crosslinking at the focal point to form PNIPAm micro-gels. Slicing and hatching distances were adjusted within a 200-400 nm range to optimize the printing parameters.

To prevent the PNIPAm hydrogel structure from being damaged by overexposure or incomplete curing due to underexposure, the laser power and scanning speed were first optimized to laser dose range to print for the printing of PNIPAm photoresists by Nanoscribe [50]. After the preliminary investigations on these two parameters, the laser powers from 25 to 45 mW, and the scanning speeds from 5,000 to 15,000  $\mu m \, s^{-1}$  were used to print PNIPAm hydrogel micro-cuboids for further observing the printed structures. The PNIPAm hydrogel micro-stripes of varying widths were printed to investigate the resolution of this hydrogel (Figure S1).

To fabricate the gradient bilayer and trilayer hydrogel micro-actuators, a user-defined subroutine programming the laser power and scanning speed for different layers across the thickness of the micro-actuators with the aid of Describe software of the Nanoscribe System. For the laser power for bilayer micro-actuators a, b, and d, the bottom layer was printed at 40 mW and the upper layer at 30 mW, respectively, which are determined based on the results of shrinkage rates and elastic moduli of the hydrogel micro-cuboids.

The trilayer hydrogel micro-actuators c and e were printed with the laser power decreasing from 40 to 30 mW from the bottom to the top. All these micro-actuators were printed at a printing speed of 10,000  $\mu$ m/s.

Before the hydrogel micro-actuators were printed, the glass coverslips were cleaned with acetone and treated with TMSPA solutions to enhance the adhesion between the glass substrates and the printed hydrogel structures. After printing, the samples were immersed in isopropanol for 24 h to remove the uncured photoresist. Subsequently, isopropanol was replaced with water to obtain the PNIPAm hydrogel micro-actuators.

## 2.4 Characterization and testing

### 2.4.1 Confocal imaging of PNIPAm hydrogel microcuboids

The swelling and shrinking behaviors of homogeneous PNIPAm micro-cuboids, printed at printing speeds ranging from 5,000 to 10,000 µm/s and laser powers from 20 to 40 mW, were investigated using a confocal laser scanning microscope (CLSM) (Leica TCS SP8, Leica, Germany). The micro-hydrogel sample printed on the glass coverslip was immersed in ultrapure water for 24 h before characterization. The petri dish containing the sample was placed in a temperature-controlled chamber (Tokai Hit chamber). Initially, the sample was imaged at room temperature, followed by heating and stabilization in the chamber at 37°C for 20 min to acquire confocal images of the shrunk hydrogel micro-cuboids. Image analysis was performed using ImageI software.

## 2.4.2 Micromechanical characterization by atomic force microscopy (AFM)

The micromechanical properties of the PNIPAm hydrogel micro-cuboids were determined by atomic force microscope (BioScope Catalyst, Bruker). The AFM was integrated with an inverted microscope (Nikon, Eclipse Ti) equipped with a 20× objective to enable visualization of the probe, facilitating precise control of tips and sample positioning. Silicon cantilevers (MLCT, Bruker) with a spring constant kof 0.03 N/m were employed for the measurements, with setup and calibration of the AFM conducted before testing. Specifically, the contact model and ScanAsyst in the fluid model were selected to evaluate hydrogel stiffness in aqueous environments. The laser positioning, AFM positioning, and cantilever calibration were carried out sequentially. Young's modulus (E) of the hydrogel sample was determined by analyzing the force (F) generated during the indentation between the probe and hydrogel. The force was calculated using the formula:  $F = k \times \delta$ , where k represents the spring constant of the cantilever, and  $\delta$  denotes the deflection of the cantilever. Data analysis was performed using the software Nanoscope Analysis 1.7. The Hertzian model was employed to fit force-indentation curves generated by the AFM for cantilevers with a pyramidal indenter. Young's moduli of hydrogel micro-cuboids were obtained from the force–indentation curves via the Nanoscope Analysis.

## 2.4.3 Characterization of AuNRs by UV-Vis and transmission electron microscope (TEM)

To confirm the light absorption properties of the PEG-modified AuNRs at 808 nm for the light actuation of PNIPAm micro-hydrogels, both the PEG-modified AuNRs and the CTAB-modified AuNRs were characterized using a UV-Vis-NIR spectrometer (PerkinElmer, USA). The light wavelength range for the testing was set from 400 to 1,180 nm.

The morphologies of CTAB-stabilized AuNRs and PEGmodified AuNRs were examined using the TEM. The samples were prepared by depositing the AuNR solutions on carbon-coated copper grids, followed by drying at room temperature. TEM imaging was conducted using the Jeol JEM-2011 microscope (Japan), operating at an accelerating voltage of 120 kV. The sizes of these AuNRs, including their lengths and diameters, were analyzed using ImageJ.

#### 2.4.4 NIR light actuation of hydrogel micro-actuators

An 808-nm laser (LSR808h-4W-FC; Lasever Inc., Ningbo, China) served as the NIR light source. The coverslip with the printed hydrogel sample was placed in the petri dish and immersed in the solution of PEG-modified AuNRs. The NIR light was used as the stimulus for actuation because of its deep penetration, minimal phototoxicity, and potential applications in biomedical fields, while UV light poses high risks of photodamage and limited penetration depth. The light source was placed 20 cm away from the sample. The laser power for the actuation of micro-actuators a-cranged from 1.50 to 2.5 W for investigating the effects of laser power on the actuation behaviors. A FLIR C3-X (FLIR System OU, Estonia) thermal camera was used to record the temperature changes during the actuation. To compare the actuation behaviors of micro-actuators a-e, the laser power of NIR light was kept the same at 2.0 W (the power density, 1.34 W cm<sup>-2</sup>). Observation of the light actuation of these micro-actuators was conducted using an optical microscope, and the videos were recorded using a CCD camera. The actuation behaviors, including the measurement of bending angles ( $\alpha$ ), curvatures ( $\kappa$ ), and calculation of the actuation time  $(t_a)$  and recovery time  $(t_r)$ , were analyzed using ImageI from the recorded videos, based on five cycles of actuation and recovery.

6 — Tongqing Li et al. DE GRUYTER

## 3 Results and discussion

## 3.1 Modification of AuNRs by PEG

The optical properties and morphologies of the PEG-modified AuNRs were characterized using UV-Vis spectroscopy and TEM. Figure 2 presents the characterization results of the AuNRs before and after modification. In the UV-Vis spectra of CTAB-stabilized AuNRs and PEG-modified AuNRs (Figure 2(a)), both spectra exhibit strong absorption peaks around 800 nm, indicative of the localized surface plasmon resonance characteristic of AuNRs. However, the absorption peak of PEG-modified AuNRs appears slightly shifted compared to CTAB-stabilized AuNRs, suggesting alterations in the optical properties due to surface modification. From the TEM images of CTAB-stabilized AuNRs and PEG-modified AuNRs (Figure 2(b) and (c)), the average aspect ratio of the PEG-modified AuNRs is approximately 3.86, slightly lower than that of CTAB-stabilized AuNRs (Table S1). This reduction in aspect ratio may result from the binding of PEG molecules to the AuNR surface, leading to alterations in nanorod dimensions. Nevertheless, despite these changes, the PEG-modified AuNRs retain their nanorod morphology and exhibit high light absorption at approximately 800 nm. Overall, these results confirm the successful modification of AuNRs with PEG, highlighting the potential for tailoring their optical and morphological properties for the application of NIR light actuation.

# 3.2 Relationship between laser dose and swelling/deswelling ability

The effect of printing laser dose on the swelling and deswelling behaviors of PNIPAm hydrogel micro-cuboids fabricated

via 2PP was investigated using CLSM. Figure 3 shows the micro-cuboids printed at different laser powers and scanning speeds, along with their corresponding shrinkage rates. In Figure 3(a) and (b), the laser power for printing each microcuboid increases from 20 to 45 mW from the left to the right, while the scanning speed increases from 5,000 to 10,000 μm/s from the bottom to the top. The sizes of micro-cuboids printed at 20 mW are slightly smaller than the designed size and are less bright compared to those printed at higher laser powers (Figure 3(a)). This is caused by incomplete curing due to the lower laser dose below the polymerization threshold of the hydrogel photoresist or the weak fluorescent signal below the LCST, especially for the edge regions. When the temperature of the sample reaches 37°C, the micro-cuboids in Figure 3(b) become smaller and brighter than those in Figure 3(a). This is because when the temperature of the sample exceeds the LCST of PNIPAm hydrogels, the hydrogel networks contract and expel water, causing the incorporated fluorescence molecules to aggregate closer, which increases the fluorescence signal intensity [51]. By analyzing the volumes of micro-cuboids at room temperature and 37°C, the volumetric changes of the PNIPAm hydrogel micro-cuboids produced at different printing settings were obtained. The relationships among shrinkage rates, scanning speed, and laser power are presented in Figure 3. In general, the shrinkage rate of PNIPAm microcuboids increases noticeably with decreasing laser power and slightly with increasing scanning speed. The maximum difference in the shrinkage rate reaches over 40% between the one printed at  $45 \, \text{mW}$ ,  $5,000 \, \mu \text{m/s}$  and the one printed at 25 mW, 10,000 µm/s. This result reveals that both higher laser power and lower scanning speed contribute to increased exposure of the photoresist to the laser, resulting in denser crosslinking of the PNIPAm hydrogel and less pronounced swelling and deswelling behaviors. These findings demonstrate that

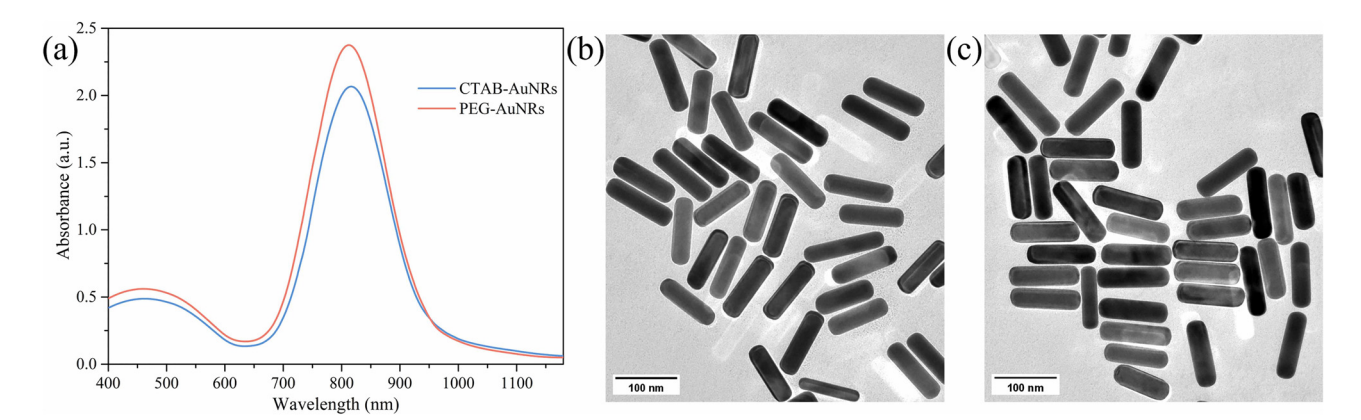
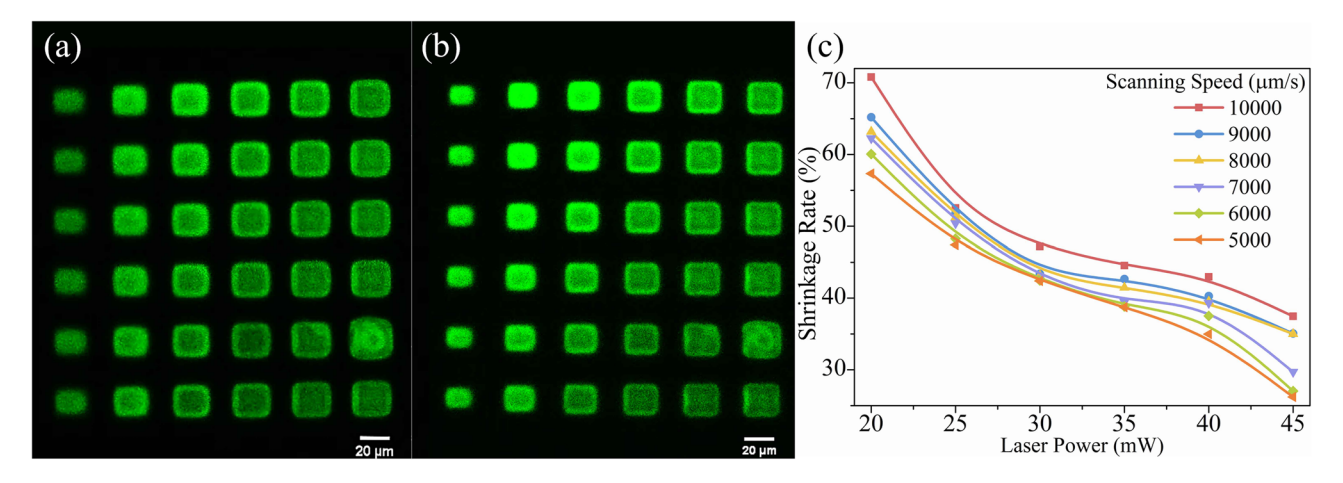


Figure 2: Characterization of the light-absorption properties and morphologies of PEG-modified and CTAB-stabilized AuNRs: (a) UV-Vis of CTAB-stabilized AuNRs and PEG-modified AuNRs; (b) TEM image of the CTAB-stabilized AuNRs; and (c) TEM image of the PEG-modified AuNRs.



**Figure 3:** The shrinkage behavior of PNIPAm hydrogel micro-cuboids printed at different laser doses. The CLSM images of PNIPAm hydrogel micro-cuboids (a) at room temperature and (b) at 37°C; and (c) the shrinkage rates of PNIPAm hydrogel micro-cuboids printed at different laser power and scanning speed.

variation in printing settings, particularly laser power, can effectively modulate the swelling and deswelling capabilities of the PNIPAm hydrogels. This fundamental understanding underpins the feasibility of one-step printing of stimulus-responsive micro-actuators with tailored functionalities.

# 3.3 Relationship between micro-mechanical properties and laser doses

The micro-mechanical properties of PNIPAm hydrogel micro-cuboids printed at varying laser powers and scanning speeds were investigated using AFM-based nanoindentation. A series of PNIPAm hydrogel micro-cuboids arranged in a 3 × 3 array

was printed using a laser power varied from 25 to 45 mW and scanning speeds ranging from 5,000 to 10,000 µm/s (Figure S2). The nanoindentation analysis was performed on these printed hydrogel micro-cuboids. The force–separation curves obtained from nanoindentation experiments were analyzed using the Hertzian model to determine Young's moduli. The force–separation curves obtained from curve fitting show the correlation between applied force and indentation depth under various printing conditions (Figure 4(a)). Young's moduli of the printed hydrogels vary with laser doses, including scanning speed and laser power (Figure 4(b)).

Young's moduli of the hydrogels significantly increase with the laser power while showing a slight decrease with the scanning speed (Figure 4(b)). For instance, at a fixed

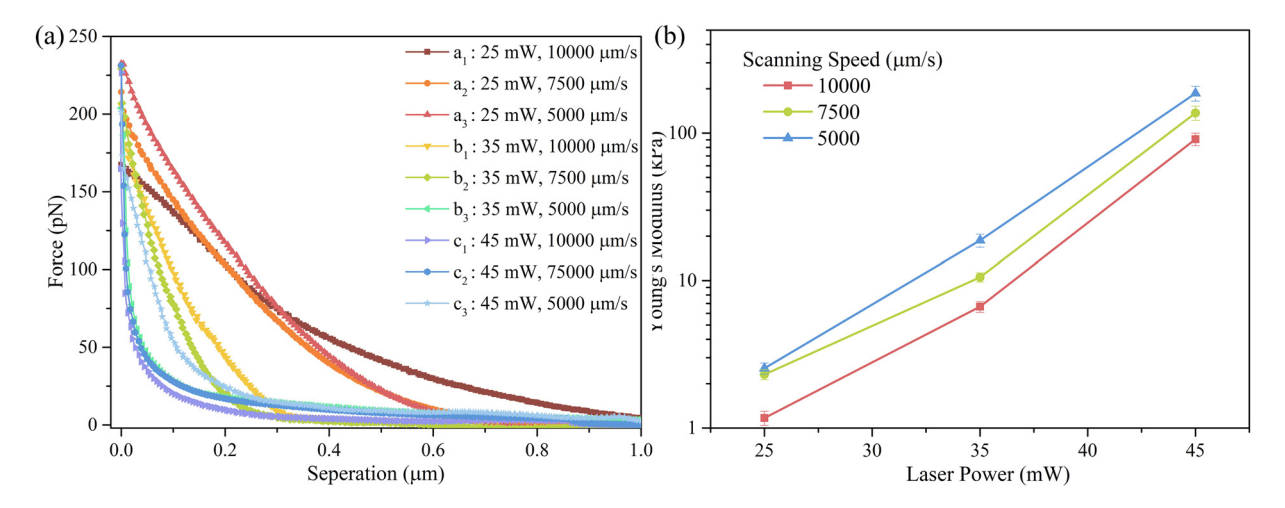


**Figure 4:** Elastic moduli of PNIPAm hydrogel micro-cuboids printed at different laser doses: (a) The fitted force–separation curves of PNIPAm hydrogel micro-cuboids printed at the scanning speed from 5,000 to 10,000 μm/s and the laser power from 25 to 45 mW; and (b) Young's moduli of the hydrogel micro-cuboids.

8 — Tongqing Li et al. DE GRUYTER

scanning speed of 10,000  $\mu m/s$ , when the laser power increases from 25 to 45 mW, Young's modulus of the hydrogels significantly increases from 1.2 to 90.4 kPa (Table S2). Moreover, maintaining a constant laser power at 35 mW while decreasing scanning speed from 10,000 to 5,000  $\mu m/s$  can lead to an increase in Young's modulus from 6.7 to 18.7 kPa but with a lesser amount. The increase in Young's moduli of the hydrogels can be attributed to their enhanced crosslinking induced by higher laser doses [45,52], thus demonstrating the potential for tailoring the mechanical behavior of hydrogels through precise control over printing parameters such as laser power.

## 3.4 NIR-light actuation behaviors of PNIPAm hydrogel micro-actuators

The actuation performance of hydrogel macro-actuators can be predicted and optimized for design purposes using simulation models *via* various methods such as residual neural networks and genetic algorithms [53,54]. However, predicting the actuation performance of micro-actuators by simulation would be challenging due to the difficulty of determining accurate model parameters such as viscoelastic properties of the micro-hydrogels. In this study, the actuation performance of the gradient hydrogel micro-

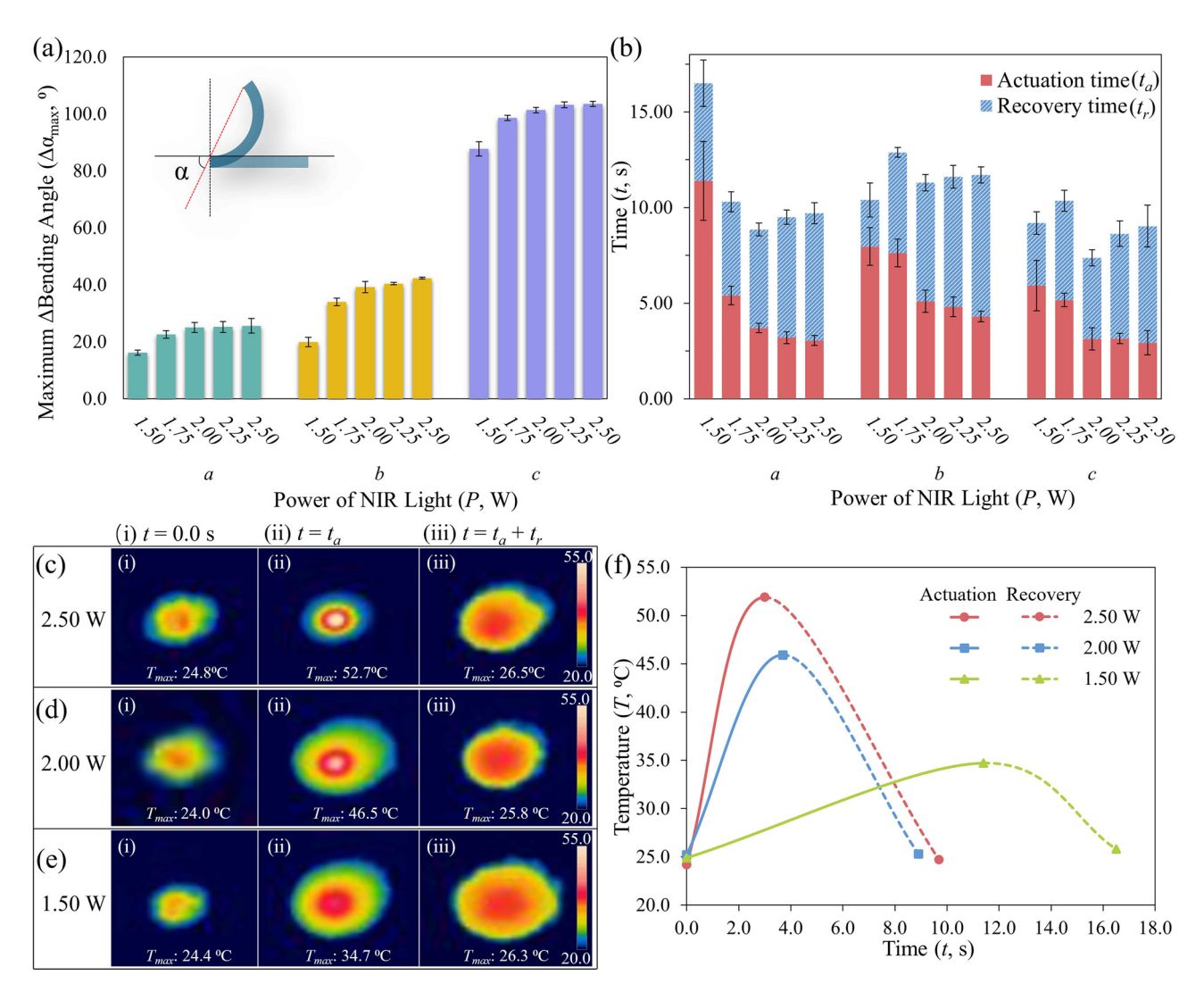


**Figure 5:** (a) Schematic for measurement of the  $\alpha$  and the  $\Delta \alpha_{\rm max}$  of PNIPAm hydrogel micro-actuators a-c at different power levels; (b) variation of the  $t_{\alpha}$  and  $t_{r}$  at different power levels; (c)–(e) thermal images of micro-actuator a during the NIR-light actuation under the light power of (c) 2.50 W, (d) 2.0 W, and (e) 1.5 W and recovery (images (i), (ii), and (iii) refer to the state of samples at the time of 0.0 s,  $t_{\alpha}$ , and  $t_{c}$  [or  $t_{\alpha} + t_{r}$ ]); and (f) temperature changes of micro-actuator a during the NIR light actuation at 2.50, 2.0, and 1.5 W (the solid lines and dotted lines indicate the actuation under the NIR light and the recovery process with the NIR light off, respectively).

actuators was assessed experimentally by investigating various factors, including the power of NIR light during the actuation, gradient structures, and sizes. The actuation behaviors investigated include the  $\alpha$ ,  $\kappa$ ,  $t_a$ , and  $t_r$ .  $\alpha$  was measured as the angle between the bent state and the original state (Figure 5(a)) [55,56]. The difference in bending angle ( $\Delta \alpha$ ) from the initial state to a certain state of actuation or recovery was calculated to present the shape change degree during the actuation and recovery. Moreover, to determine the shape-changing capability of the micro-actuators, the maximum values of the difference in bending angle change ( $\Delta \alpha_{\text{max}}$ ) were compared. Meanwhile,  $t_a$  and  $t_r$  were adopted to evaluate the shape-morphing speed. The  $t_a$  refers to the duration from exposure to NIR light until  $\Delta \alpha$  reaches its maximum, while  $t_r$  denotes the time taken for the microactuator to return to its original state upon the light being turned off. Additionally, the cycle time of actuation and recovery  $(t_c = t_a + t_r)$  was used to evaluate the overall actuation and recovery speed.

### 3.4.1 Effects of laser power of NIR light on actuation behaviors

The power of the NIR laser could affect actuation behaviors such as  $\alpha$ ,  $t_a$ , and  $t_r$ . The bending behaviors of the gradient bilayer micro-actuators a and b and the gradient trilayer micro-actuator c were investigated across a range of laser powers from 2.50 to 1.50 W. When the laser power increases from 1.50 to 1.75 W, the  $\Delta \alpha_{\rm max}$  increases apparently, but when the laser power further increases, there is only a slight increase in  $\Delta \alpha_{\text{max}}$  (Figure 5(a)). Meanwhile, in Figure 5(b), with the increase of laser power, their  $t_a$  values decrease while the  $t_r$  values increase. Particularly, the  $t_c$  values of these micro-actuators reach their minimum values at the laser power of 2.00 W, which can serve as the optimum laser power for the micro-actuator to achieve a larger  $\Delta a_{max}$  and a shorter  $t_c$  as compared with other conditions.

The influence of laser power on the actuation behaviors of the 4D-printed micro-actuators is related to the photothermal performance and thermal dissipation of the AuNRs solution. To investigate this relationship, micro-actuator a was selected to observe the temperature changes during its NIR-light actuation and recovery at three different laser powers (Figure 5(c)-(e)). Figure 5(c)(i)-(e)(i) correspond to the states before exposure to NIR light (i.e.,  $t = 0.0 \, \text{s}$ ), with the maximum temperatures in the center of the light spot recorded around 24.0°C. Under the NIR light exposure, respectively, when maximum bending angle achieving their maximum bending angles (Figure 5(c)(ii)–(e)(ii)), the temperatures reach a maximum at 52.7, 46.5, and 34.7°C for the light power

of 2.5, 2.0, and 1.5 W, respectively. Upon turning off the NIR light, the temperature gradually declines to near room temperature. Notably, as the laser power is reduced from 2.50 to 1.50 W, the peak temperature decreases from 52.7 to 34.7°C (Figure 5(f)). Concurrently,  $t_a$  increases from approximately 3.0 to 12.0 s, while  $t_r$  decreases from nearly 7.0 to 5.0 s.

These results suggest that a higher NIR laser power accelerates the actuation but reduces the recovery time. Conversely, low laser powers, such as 1.75 and 1.50 W, fail to fully actuate the micro-actuators to their maximum bending angles. Particularly at the laser power of 1.50 W, the maximum temperature in the central spot of the lightexposed area is 34.7°C, just above the LCST of PNIPAm hydrogels. The temperature gradually decreases from the center to the edge of the light spot due to the gradient distribution of laser energy density and heat transfer in the aqueous solution [57]. Consequently, although the microactuator exhibits slight bending behavior, the maximum temperature remains higher than the LCST of PNIPAm [58]. The heat generated by the photothermal effects of AuNRs dissipates in the outer area, preventing further shrinkage of the PNIPAm hydrogel micro-actuator to its most bent state. When the laser power is above 1.75 W, the center temperature of the micro-actuator would be much higher than the LCST of PNIPAm, so it rapidly shrinks and leads to its maximum bending. However, at high laser power levels such as 2.25 and 2.50 W, the high temperatures when the micro-actuator reaches its maximum bending angle result in a slow cooling and recovery. Therefore, to achieve both a higher bending angle and a shorter cycle time of actuation and recovery for the micro-actuator, a power of 2.00 W was chosen as the optimum NIR laser power for investigating the effects of size and layer thickness on the actuation behaviors of micro-actuators a-e.

### 3.4.2 Effects of size and layer thickness on actuation behaviors

Although the NIR laser power could affect the actuation behaviors of the hydrogel-based micro-actuators, their actuation capabilities were determined by their sizes and layer thickness. The effects of length, overall thickness, and layer thickness on the actuation behaviors, including  $\Delta \alpha_{max}$ ,  $t_a$ ,  $t_r$ , and  $\Delta \kappa_{\rm max}$  (the maximum value of the difference of the curvature between the original state and the most bent state) of micro-actuators a-e under the NIR laser power of 2.00 W were investigated. Since the side-view optical images of the micro-actuator cannot depict the bending behavior (Figure S3), the top-view optical images of the micro-actuators a-e in Figure 6(a)-(e) are used to evaluate their bending

degree during the one-cycle NIR-light actuation and recovery. The actuation behavior of each micro-actuator over two cycles is presented in Video S1. The performance was evaluated over five consecutive actuation-recovery cycles, with no noticeable decline in actuation efficiency observed (Figure S4). The as-printed hydrogel micro-actuators show different degrees of bending angles during exposure to the NIR laser. Their bending results from their heterogeneous structures with the differences in crosslinking density induced by varying laser doses during printing. It is found that the bending direction is dominated by the elastic modulus [59], with all these micro-actuators bending toward the layer printed with a higher laser dose and, namely, with a higher elastic modulus. Although the densely crosslinked PNIPAm hydrogel layer exhibits lower shrinkage, its Young's modulus is significantly higher than that of the sparsely crosslinked layer, as indicated by the nanoindentation results in Section 3.3. Within a hydrogel micro-actuator, the layer with a high elastic modulus shows much higher bending stiffness than the one with a low elastic modulus. If their bending is regarded as the bending of a cantilever beam, the bending behavior can be explained by the equation of bending

$$\frac{F}{\delta} = \frac{\text{CEI}}{L^3},$$
 (1)

where F is the actuation force, C is the constant,  $\delta$  is the deflection, E is the elastic modulus, I is the second moment area or the moment of inertia, and L is the length of the micro-actuator.

Since the cross-section of these micro-actuators is a rectangle, the moment of inertia can be given by

$$I = b \times \frac{h^3}{12},\tag{2}$$

where *b* and *h* are the width and the thickness of the microactuator, respectively [60].

For a single micro-actuator, the moment of inertia and lengths of different layers are the same. From equation (1), under the same load, the layer with high elasticity would show less displacement, so the layer with high elasticity lies in the inner layer of the bent micro-actuator. For the other aspect, the shrinkage of the hydrogel network, the hydrogel layer printed at a lower laser dose exhibits a higher volumetric contraction rate, which can occur along both length and thickness. Although the lengthwise shrinkage of the sparsely crosslinked layer is partially constrained by the high bending

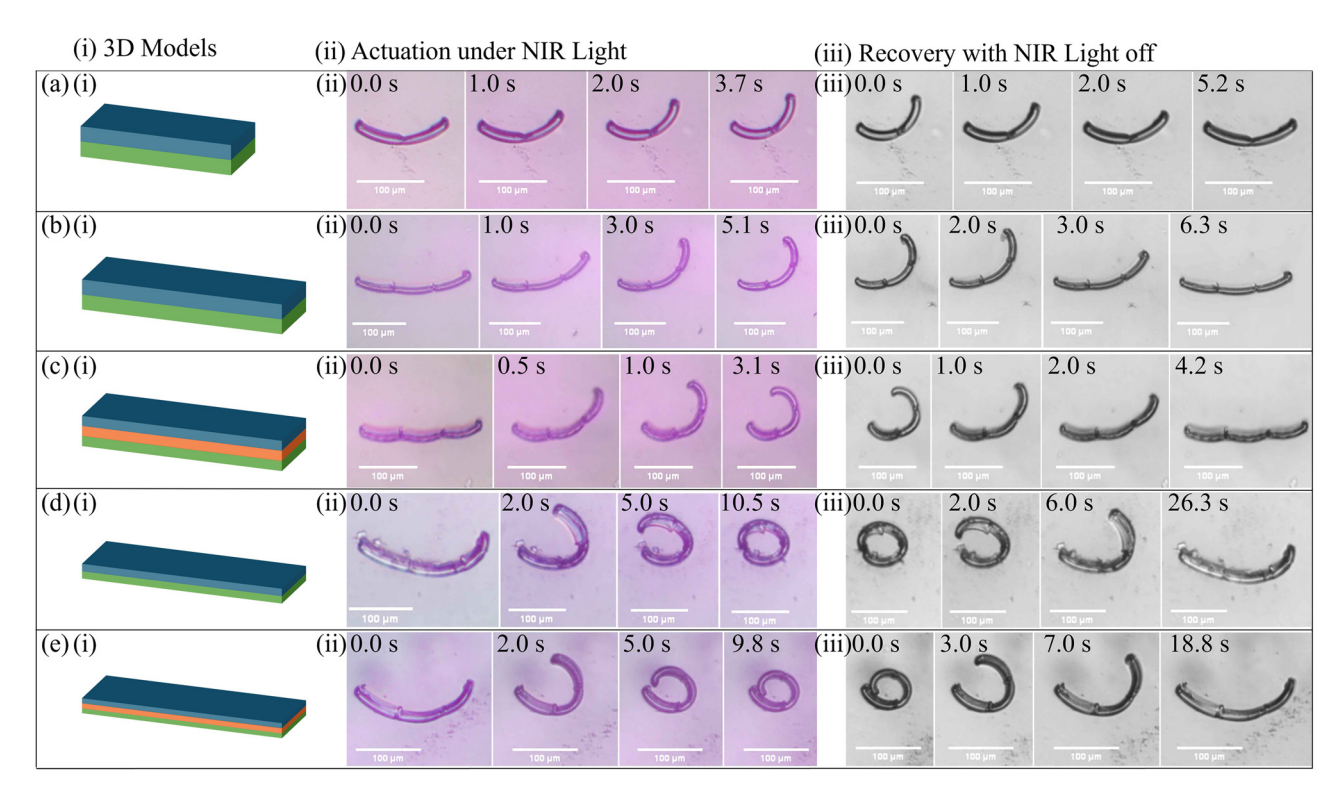


**Figure 6:** 3D models, NIR-light actuation, and recovery of micro-actuators with varying sizes and layer thicknesses. (a)–(e) corresponds to micro-actuators a-e; (a)(ii)–(e)(ii) 3D models for printing of micro-actuators a-e; (a)(iii)–(e)(iii) the NIR-light actuation process of micro-actuators a-e; (a)(iii)–(e) (iii) the recovery process of micro-actuators a-e with the NIR light off.

stiffness of the densely crosslinked layer, the contraction in thickness compensates for the overall shrinkage. This revealed that the bending mechanism is essential for designing and printing the gradient micro-actuators with specified bending directions, particularly in complex hydrogel structures.

The variation in parameters evaluating the bending behaviors of micro-actuators a–e, including the  $\Delta \alpha$ ,  $\Delta \kappa$  during the actuation and recovery, as well as  $\Delta \alpha_{\rm max}$ ,  $\Delta \kappa_{\rm max}$ ,  $t_a$ , and  $t_r$ , are shown in Figure 7. The values of  $\Delta \alpha_{\rm max}$ ,  $\Delta \kappa_{\rm max}$ ,  $t_a$ , and  $t_r$  of these micro-actuators are also listed in Table 2. The differences in the actuation behaviors of the micro-actuators resulting from the variation in their length, overall thickness, and layer thickness are elucidated below.

#### 3.4.2.1 Effect of length variation

The gradient bilayer micro-actuators a and b have lengths of 150 and 225  $\mu$ m, respectively, with the lower and upper

layers printed at the laser dose of 40 and 30 mW. The longer micro-actuator b shows higher values of  $\Delta a_{max}$ and  $\Delta \kappa_{max}$  as compared with the shorter micro-actuator a, namely increasing from 25.0° to 39.2° and from 0.0093 to 0.0138  $\mu m^{-1}$ , respectively. The higher curvature  $\Delta \kappa_{max}$  of the longer micro-actuator b during actuation is attributed to the increased arc length of its bent state compared with micro-actuator a [61]. However, the length increase also results in longer actuation and recovery, with the  $t_a$  value rising from 3.7 to 5.1 s, and the  $t_r$  value increasing from 5.2 to 6.3 s separately. Given that both micro-actuators a and b have identical thickness and their upper and lower layers were printed at the same laser dose, the shrinkage speed is also uniform because of the consistent crosslinking in each layer and the water repulsion properties of the PNIPAm hydrogel network [62]. The increased actuation and recovery time for the longer micro-actuator is due to the greater distance the free end needs to travel to reach the maximum

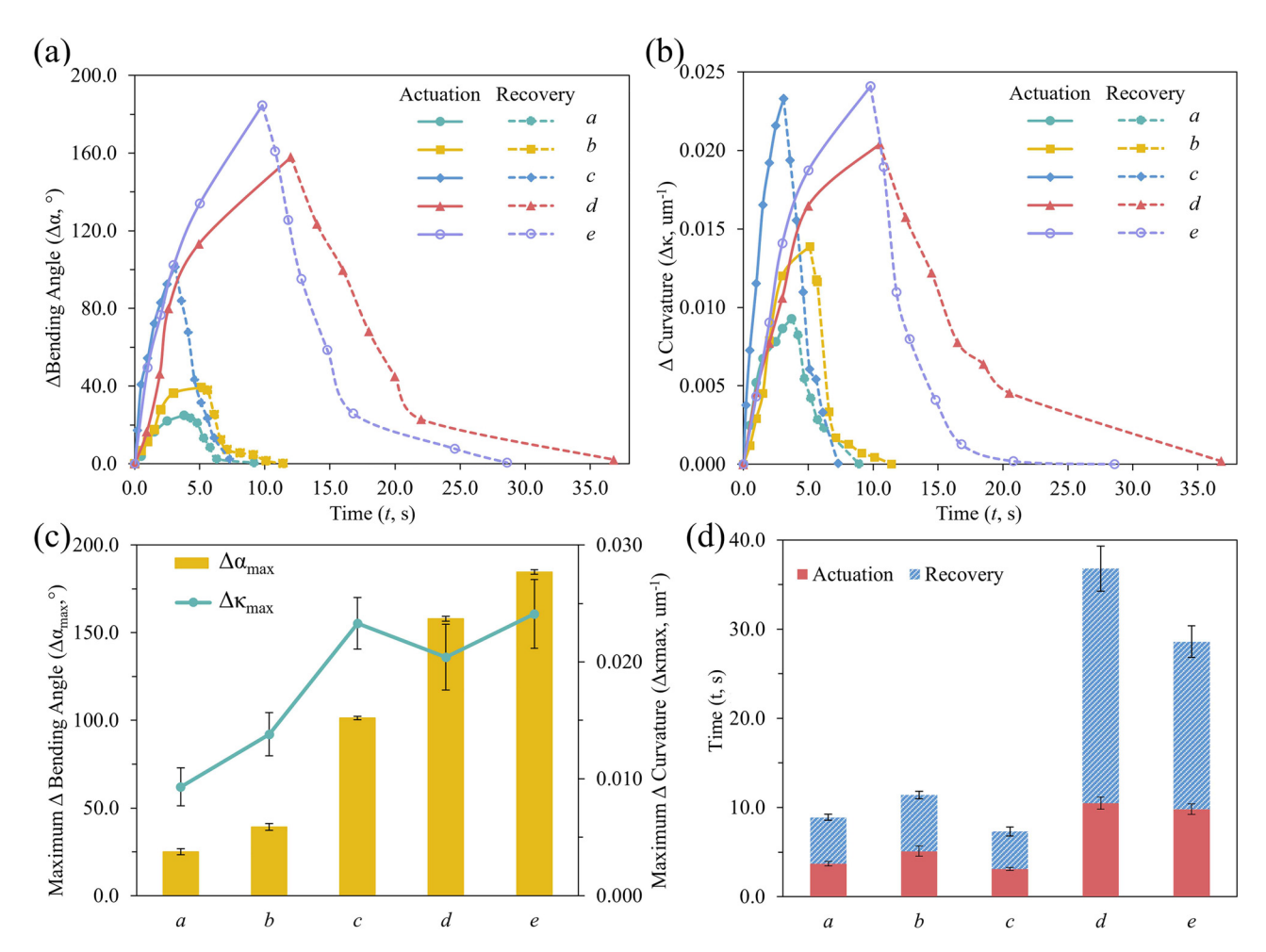


**Figure 7:** The actuation behaviors of micro-actuators a-e: (a) the bending angle changes and (b) the curvature changes of micro-actuator a-e during the NIR-light actuation and recovery; (c) the comparison of maximum bending angle and curvature of micro-actuator a-e; and (d) the comparison of actuation time and recovery time of micro-actuator a-e.

**Table 2:** Comparison of maximum  $\Delta$  bending angle, maximum  $\Delta$  curvature, actuation time, and recovery time of micro-actuators  $\alpha$ -e

Name of micro- actuators	Maximum $\Delta$ bending angle ( $\Delta \alpha_{max}$ , 0)	Maximum Δ curvature (Δκ <sub>max</sub> , μm <sup>-1</sup> )	Actuation time $(t_a, s)$	Recovery time $(t_r, s)$
а	25.0 ± 1.73	0.0093 ± 0.0016	3.7 ± 0.25	5.2 ± 0.34
b	39.2 ± 1.99	0.0138 ± 0.0018	5.1 ± 0.58	6.3 ± 0.42
С	101.3 ± 0.98	0.0233 ± 0.0021	3.1 ± 0.16	4.2 ± 0.50
d	157.9 ± 1.47	0.0204 ± 0.0028	10.5 ± 0.67	26.3 ± 2.53
е	184.6 ± 1.21	0.0241 ± 0.0029	9.8 ± 0.59	18.8 ± 1.76

bending angle and return to the original position. These results indicate that increasing the length is a method to fabricate the micro-actuator with a large bending angle despite slightly slowing down the actuation and recovery.

#### 3.4.2.2 Effect of thickness variation

The effect of thickness variation on the actuation behaviors of the micro-actuators b-e, all with a length of 225  $\mu$ m, is summarized as shown in Table 2. When the thickness decreases from 12 to 6 µm, both the gradient bilayer micro-actuator d shows higher values of  $\Delta \alpha_{\max}$  and  $\Delta \kappa_{\max}$ as compared with the gradient bilayer micro-actuator b, namely increasing from 39.2° to 157.9° and from 0.0138 to 0.0204 µm<sup>-1</sup>, respectively. Similarly, the gradient trilayer micro-actuator e also exhibits higher values of  $\Delta \alpha_{max}$  and  $\Delta \kappa_{max}$  as compared with the gradient trilayer micro-actuator c, namely rising from 101.3° to 184.6° and from 0.0233 to 0.0241 μm<sup>-1</sup>, correspondingly. The thicker gradient bilayer micro-actuators b and trilayer micro-actuator c show lower maximum bending angles and curvature correspondingly as compared with the micro-actuator d and e because of the higher moment of inertia for a thicker cross-section according to equation (2). However, the decrease in the overall thickness also slows the actuation and recovery process, specifically, the  $t_a$  and  $t_r$  values for the gradient bilayer micro-actuators increasing from 5.1 to 10.5 s and from 6.3 to 26.3 s, respectively, and the  $t_a$  and  $t_r$  values for the gradient trilayer micro-actuators rising from 3.1 to 9.8 s and from 4.2 to 18.8 s, respectively. The thinner gradient bilayer and trilayer micro-actuators b and c show slower actuation and recovery mainly because of the longer trajectory for their free ends to reach the maximum bending angles.

#### 3.4.2.3 Effect of varying layer thickness

The impact of varying layer thickness on their actuation behaviors is assessed by comparing 12- $\mu$ m-thickness micro-actuators b and c, as well as the 6- $\mu$ m-thickness micro-actuators d and e. The individual layer thicknesses

of micro-actuators b, c, d, and e are 6, 4, 3, and 2 µm, respectively, exceeding the resolution (~0.8 µm) of the printed PNIPAm hydrogel stripes (Figure S1). The bilayer gradient micro-actuators b and d were separately printed at 40 and 30 mW for the lower and upper layers, while the laser powers for the printing of lower, intermediate, and upper layers of triple-layered gradient micro-actuators c and e were 40, 35, and 30 mW, respectively. The variation from a bilayer to trilayer gradient structure leads to a significant increase in  $\Delta \alpha_{\rm max}$ , namely from 39.2° to 101.3° for micro-actuators b and c and from 157.9° to 184.6° for the micro-actuators d and e, respectively. Similarly, the  $\Delta \kappa_{max}$  increases from 0.0138 to  $0.0233 \, \mu \text{m}^{-1}$  for the micro-actuators b and c and from 0.0204 to  $0.0241 \,\mu\text{m}^{-1}$  for the micro-actuators d and e, respectively. The  $t_a$  are reduced by 2.0 and 0.7 s, and  $t_r$  decreases by 2.0 and 7.5 s, correspondingly. For the 12-µm-thickness micro-actuators b and c, when the layer thickness decreases from 6 to 4  $\mu m$ , the  $\Delta \alpha_{max}$  and  $\Delta \kappa_{max}$  increase by over 150 and nearly 70%, respectively, and the cycle time of actuation and recovery shortens by about 35%. Similarly, for the 6-µmthickness micro-actuators d and e, when the layer thickness decreases from 3 to 2  $\mu$ m, the  $\Delta \alpha_{max}$  and  $\Delta \kappa_{max}$  increase by 17 and 18%, respectively, and the cycle time of actuation and recovery shortens by about 22%. These results indicate that decreasing layer thickness enhances the bending angle and accelerates both the actuation and recovery processes. This is because a more gradual crosslinking gradient within the trilayer hydrogel structure leads to a more uniform and continuous stress distribution [63]. The gradient trilayer structure, with an intermediate layer, also facilitates a gradual transition in crosslinking density and elastic modulus across layers, reducing internal stress and improving actuation amplitude and speed. In contrast, the sharp change in the elastic modulus at the interface in the gradient bilayer structure increases the internal stress, resulting in rougher and slower actuation and recovery [64]. It is noted that the micro-actuator e exhibits the largest bending degree change (over 180°) among these micro-actuators as the layer thickness is the minimum at 2 µm and the crosslinking within the micro-structure varies at 2-µm level. Theoretically, the minimum layer thickness can be designed as the hatching distance (generally less than 1 µm) to fabricate the gradient structure with the sub-microscale crosslinking gradient and multilayer gradient microstructures.

Overall, increasing the length and decreasing the overall thickness of the micro-actuators enhance the bending angles and curvature but slow down the actuation and recovery. Reducing the layer thickness in gradient hydrogel structures is also favorable for increasing the bending angles and expediting the actuation and recovery processes. This study was among the first attempts to demonstrate the applicability of the programming-based gradient crosslinking strategy for fabricating the hydrogel micro-actuators with enhanced bending performance achieved in the trilayer structure over the bilayer one. Moreover, using this gradient printing strategy, the micro-actuators could be fabricated in a onestep and one-material process. Compared with multi-material printing, this gradient printing method simplifies the fabrication process and alleviates issues of the interfacial adhesion between different materials.

## 4 Conclusion

In conclusion, the 2PP-based 4D printing coupled with the innovative gradient printing strategy has been demonstrated to be capable of fabricating stimulus-responsive hydrogel micro-actuators with different bending performance. With the developed gradient printing strategy, the micro-actuators with gradient variations in cross-linking densities and, thus, mechanical behaviors across their thickness were realized by creating a user-defined subroutine programming the laser dose and scanning speed of different layers. Among the various studied factors, including NIR laser power, length, thickness, and the number of layers of the micro-actuators, it was found that the number of layers played the most significant role in enhancing the actuation performance. From the bilayer to the gradient trilayer, the maximum bending angle and curvature change increased by over 150% and nearly 70%, respectively, and the cycle time of actuation and recovery shortened by about 35%. This gradient printing strategy overcomes the challenges associated with multi-material printing, such as complex printing procedures and interfacial adhesion issues. The as-printed gradient micro-actuators highlight the versatility of this technique, opening avenues for applications in fields such as soft robotics, biomedical devices, and microfluidics. Furthermore, this technique holds great potential for developing universal strategies for printing gradient multilayer microstructures across various materials. Future research

could explore the gradient printing of other materials and micro-actuators with complex functions and other materials, as well as the applications of the micro-actuators.

**Funding information:** The authors would like to express sincere thanks to the financial support from the Research Committee of The Hong Kong Polytechnic University (Project codes: RHFV and G-UARR). The work described in this article was partially supported by a grant from the Research Grants Council of the Hong Kong Special Administrative Region, China (Project Nos. PolyU15211221 and PolyU15212523).

Author contributions: All authors have accepted responsibility for the entire content of this manuscript and approved its submission.

**Conflict of interest:** The authors state no conflict of interest.

Data availability statement: The datasets generated and/ or analyzed during the current study are available from the corresponding author on reasonable request.

## References

- Saadli M, Braunmiller DL, Mourran A, Crassous JJ. Thermally and magnetically programmable hydrogel microactuators. Small. 2023;19(16):2207035.
- Tibbits S. 4D printing: multi-material shape change. Archit Des. 2014;84(1):116-21.
- Xu J, Chen L, Yang X, Liu Z, Song Q. Mechanical and heat transfer properties of 4D-printed shape memory graphene oxide/epoxy acrylate composites. Nanotechnol Rev. 2022;11(1):3138-54.
- Deng C, Liu Y, Fan X, Jiao B, Zhang Z, Zhang M, et al. Femtosecond laser 4D printing of light-driven intelligent micromachines. Adv Funct Mater. 2023;33(11):2211473.
- Zhang Y, Raza A, Xue YQ, Yang G, Hayat U, Yu J, et al. Waterresponsive 4D printing based on self-assembly of hydrophobic protein "Zein" for the control of degradation rate and drug release. Bioact Mater. 2023;23:343-52.
- Luo K, Wang L, Wang MX, Du R, Tang L, Yang KK, et al. 4D printing [6] of biocompatible scaffolds via in situ photo-crosslinking from shape memory copolyesters. ACS Appl Mater Interfaces. 2023;15(37):44373-83.
- Cecchini L, Mariani S, Ronzan M, Mondini A, Pugno NM, Mazzolai B. 4D printing of humidity-driven seed inspired soft robots. Adv Sci. 2023;10(9):2205146.
- Hu Q, Rance GA, Trindade GF, Pervan D, Jiang L, Foerster A, et al. The influence of printing parameters on multi-material two-photon polymerisation based micro additive manufacturing. Addit Manuf. 2022:51:102575.
- Tyagi M, Spinks GM, Jager EW. 3D printing microactuators for soft microrobots. Soft Robot. 2021;8(1):19-27.

- [10] Sanchez Noriega JL, Chartrand NA, Valdoz JC, Cribbs CG, Jacobs DA, Poulson D, et al. Spatially and optically tailored 3D printing for highly miniaturized and integrated microfluidics. Nat Commun. 2021;12(1):5509.
- [11] Guo Y, Chen S, Sun L, Yang L, Zhang L, Lou J, et al. Degradable and fully recyclable dynamic thermoset elastomer for 3D-printed wearable electronics. Adv Funct Mater. 2021;31(9):2009799.
- [12] Liu X, Wei M, Wang Q, Tian Y, Han J, Gu H, et al. Capillary-forcedriven self-assembly of 4D-printed microstructures. Adv Mater. 2021;33(22):2100332.
- [13] Spiegel CA, Hackner M, Bothe VP, Spatz JP, Blasco E. 4D printing of shape memory polymers: from macro to micro. Adv Funct Mater. 2022;32(51):2110580.
- [14] Gregg A, De Volder M, Baumberg JJ. Kinetics of light-Responsive CNT/PNIPAM hydrogel microactuators. Small. 2023;20(9):2305034.
- [15] Shi H, Deng Y, Shi Y. Cellulose-based stimuli-responsive anisotropic hydrogel for sensor applications. ACS Appl Nano Mater. 2023;6(13):11524–30.
- [16] Jang S, Park S. 4D printed untethered milli-gripper fabricated using a biodegradable and biocompatible electro-and magneto-active hydrogel. Sens Actuator B-Chem. 2023;384:133654.
- [17] Li T, Huang Z, Tsui GCP, Tang CY, Deng Y. Recent advances in 4D printing of hydrogels. Rev Adv Mater Sci. 2024;63(1):20240028.
- [18] Gu X, Chen X, Tang X, Zhou Z, Huang T, Yang Y, et al. Pure-silk fibroin hydrogel with stable aligned micropattern toward peripheral nerve regeneration. Nanotechnol Rev. 2021;10(1):10–9.
- [19] Ma S, Xue P, Tang Y, Bi R, Xu X, Wang L, et al. Responsive soft actuators with MXene nanomaterials. Respons Mater. 2024;2(1):e20230026.
- [20] Xu X, Zeng Y, Chen Z, Yu Y, Wang H, Lu X, et al. Chitosan-based multifunctional hydrogel for sequential wound inflammation elimination, infection inhibition, and wound healing. Int J Biol Macromol. 2023;235:123847.
- [21] Shen X, Li S, Zhao X, Han J, Chen J, Rao Z, et al. Dual-crosslinked regenerative hydrogel for sutureless long-term repair of corneal defect. Bioact Mater. 2023;20:434–48.
- [22] Roy K, Jiang S, Jin EJ, Park SY. pH-sensitivity of a hybrid ionotronic device-based self-diagnostic hydrogel for sensing and therapeutic activity. Chem Eng I. 2023;475:146168.
- [23] Shang H, Yang X, Liu H. Temperature-responsive hydrogel prepared from carboxymethyl cellulose-stabilized Nvinylcaprolactam with potential for fertilizer delivery. Carbohydr Polym. 2023;313:120875.
- [24] Huang X, Xu L, Yu X, Li Y, Huang Z, Xu R, et al. Near-infrared light-responsive multifunctional hydrogel releasing peptide-functionalized gold nanorods sequentially for diabetic wound healing. J Colloid Interface Sci. 2023;639:369–84.
- [25] Zhang YF, Du FP, Chen L, Yeung KW, Dong Y, Law WC, et al. Supramolecular ionic polymer/carbon nanotube composite hydrogels with enhanced electromechanical performance. Nanotechnol Rev. 2020;9(1):478–88.
- [26] Podstawczyk D, Nizioł M, Szymczyk P, Wiśniewski P, Guiseppi-Elie A. 3D printed stimuli-responsive magnetic nanoparticle embedded alginate-methylcellulose hydrogel actuators. Addit Manuf. 2020;34:101275.
- [27] Ma S, Xue P, Valenzuela C, Zhang X, Chen Y, Liu Y, et al. Highly stretchable and conductive mxene-encapsulated liquid metal hydrogels for bioinspired self-sensing soft actuators. Adv Funct Mater. 2024;34(7):2309899.

- [28] Lai YP, Li Z, Naguib H, Diller E. Hybrid hydrogel-magnet actuators with pH-responsive hydrogels for gastrointestinal microrobots. Adv Eng Mater. 2023;25(20):2301060.
- [29] Mendez K, Whyte W, Freedman BR, Fan Y, Varela CE, Singh M, et al. Mechanoresponsive drug release from a flexible, tissue-adherent, hybrid hydrogel actuator. Adv Mater. 2024;36:2303301.
- [30] Ji ZY, Yan CY, Yu B, Zhang XQ, Cai MR, Jia X, et al. 3D printing of hydrogel architectures with complex and controllable shape deformation. Adv Mater Technol. 2019;4(4):1800713.
- [31] Hua M, Wu D, Wu S, Ma Y, Alsaid Y, He X. 4D printable tough and thermoresponsive hydrogels. ACS Appl Polym Mater. 2020;13(11):12689–97.
- [32] Chen L, Zhang Y, Zhang K, Li F, Duan G, Sun Y, et al. Multi-stimuli responsive, shape deformation, and synergetic biomimetic actuator. Chem Eng J. 2024;480:148205.
- [33] Fournié V, Venzac B, Trevisiol E, Foncy J, Roul J, Assié-Souleille S, et al. A microfluidics-assisted photopolymerization method for high-resolution multimaterial 3D printing. Addit Manuf. 2023;72:103629.
- [34] Zheng J, Yu H, Zhang Y, Wang J, Guo H, Luo H, et al. 4D printed soft microactuator for particle manipulation via surrounding medium variation. Small. 2024;20:2311951.
- [35] Zhang C, Lu X, Fei G, Wang Z, Xia H, Zhao Y. 4D printing of a liquid crystal elastomer with a controllable orientation gradient. ACS Appl Mater Interfaces. 2019;11(47):44774–82.
- [36] Jin D, Chen Q, Huang TY, Huang J, Zhang L, Duan H. Four-dimensional direct laser writing of reconfigurable compound micromachines. Mater Today. 2020;32:19–25.
- [37] Zorzetto L, Andena L, Briatico-Vangosa F, De Noni L, Thomassin J-M, Jérôme C, et al. Properties and role of interfaces in multimaterial 3D printed composites. Sci Rep. 2020;10(1):22285.
- [38] Wang Z, Wang D, Li X, Yang F, Liu D, Chen F. Simultaneous polymerization constructing Hydrogel-Elastomer composites with ultra-tough interface for robust epidermal mechanoreceptor. Chem Eng J. 2023;476:146564.
- [39] Li J, Zhang G, Cui Z, Bao L, Xia Z, Liu Z, et al. High performance and multifunction moisture-driven Yin-Yang-interface actuators derived from polyacrylamide hydrogel. Small. 2023;19(38):2303228.
- [40] Mao A, Fan P, Constantin L, Li N, Huang X, Cui B, et al. Forming three-dimensional micro-objects using two-dimensional gradient printing. Appl Mater Today. 2022;28:101538.
- [41] Kokkinis D, Bouville F, Studart AR. 3D printing of materials with tunable failure via bioinspired mechanical gradients. Adv Mater. 2018;30(19):1705808.
- [42] Huang TY, Huang HW, Jin D, Chen Q, Huang J, Zhang L, et al. Four-dimensional micro-building blocks. Sci Adv. 2020;6(3):eaav8219.
- [43] Jian B, Li H, He X, Wang R, Yang HY, Ge Q. Two-photon polymerization-based 4D printing and its applications. Int J Extreme Manuf. 2023;6(1):012001.
- [44] Huang Z, Tsui GCP, Deng Y, Tang CY. Two-photon polymerization nanolithography technology for fabrication of stimulus-responsive micro/nano-structures for biomedical applications. Nanotechnol Rev. 2020;9(1):1118–36.
- [45] Spratte T, Geiger S, Colombo F, Mishra A, Taale M, Hsu LY, et al. Increasing the efficiency of thermoresponsive actuation at the microscale by direct laser writing of PNIPAM. Adv Mater Technol. 2023;8(1):2200714.
- [46] Nishiguchi A, Zhang H, Schweizerhof S, Schulte MF, Mourran A, Moller M. 4D printing of a light-driven soft actuator with

- programmed printing density. ACS Appl Mater Interfaces. 2020;12(10):12176–85.
- [47] Schulz F, Friedrich W, Hoppe K, Vossmeyer T, Weller H, Lange H. Effective PEGylation of gold nanorods. Nanoscale. 2016;8(13):7296–308.
- [48] Pan Y, Liu Y, Yang S, Zhang C, Ullah ZJ. Recent research progress on the stimuli-responsive smart membrane: A review. Nanotechnol Rev. 2023;12(1):20220538.
- [49] Li M, Bae JJ. Programmable dual-responsive actuation of singlehydrogel-based bilayer actuators by photothermal and skin layer effects with graphene oxides. Adv Mater Interfaces. 2023;10(33):2300169.
- [50] Yeung KW, Dong Y, Chen L, Tang CY, Law WC, Tsui GCP, et al. Printability of photo-sensitive nanocomposites using two-photon polymerization. Nanotechnol Rev. 2020;9(1):418–26.
- [51] Li Z, Sun D, Yang J, Shang S, Wang L, Li H, et al. 3D printed heterogeneous bilayer temperature-responsive hydrogel with multi-curvature deformation. Polymer. 2024;296:126701.
- [52] Song D, Husari A, Kotz-Helmer F, Tomakidi P, Rapp BE, Rühe J. Twophoton direct laser writing of 3D scaffolds through C, H-insertion crosslinking in a one-component material system. Small. 2024;20(17):2306682.
- [53] Jin L, Yu S, Cheng J, Ye H, Zhai X, Jiang J, et al. Machine learning driven forward prediction and inverse design for 4D printed hierarchical architecture with arbitrary shapes. Appl Mater Today. 2024;40:102373.
- [54] Jin L, Zhai X, Jiang J, Zhang K, Liao W-H. Optimizing stimuli-based 4D printed structures: a paradigm shift in programmable material response. In Sensors and Smart Structures Technologies for Civil, Mechanical, and Aerospace Systems 2024. SPIE; 2024.
- [55] Dong Y, Yeung KW, Law WC, Tsui GCP, Xie X, Tang CY. Towards a consistent methodology for testing the electromechanical

- performance of strip polymer composite actuators. Polym Test. 2022:106:107463.
- [56] Simińska-Stanny J, Nizioł M, Szymczyk-Ziółkowska P, Brożyna M, Junka A, Shavandi A, et al. 4D printing of patterned multimaterial magnetic hydrogel actuators. Addit Manuf. 2022;49:102506.
- [57] Yang Z, Zhao F, Zhang W, Yang Z, Luo M, Liu L, et al. Degradable photothermal bioactive glass composite hydrogel for the sequential treatment of tumor-related bone defects: From antitumor to repairing bone defects. Chem Eng J. 2021;419:129520.
- [58] Fu H, Xue K, Zhang Y, Xiao M, Wu K, Shi L, et al. Thermoresponsive hydrogel-enabled thermostatic photothermal therapy for enhanced healing of bacteria-infected wounds. Adv Sci. 2023;10(11):2206865.
- [59] Hippler M, Blasco E, Qu J, Tanaka M, Barner-Kowollik C, Wegener M, et al. Controlling the shape of 3D microstructures by temperature and light. Nat Commun. 2019;10(1):232.
- [60] Mailen RW, Long RM, Parmar K, Indaco M, Guzzetti D. Quantifying hinge torque in self-folding, shape memory polymer origami under varying thermal loads. Appl Mater Today. 2023;35:101949.
- [61] Qu G, Huang J, Li Z, Jiang Y, Liu Y, Chen K, et al. 4D-printed bilayer hydrogel with adjustable bending degree for enteroatmospheric fistula closure. Mater Today Bio. 2022;16:100363.
- [62] Ni C, Chen D, Wen X, Jin B, He Y, Xie T, et al. High speed underwater hydrogel robots with programmable motions powered by light. Nat Commun. 2023;14(1):7672.
- [63] Käpylä E, Delgado SM, Kasko AMJ. Shape-changing photodegradable hydrogels for dynamic 3D cell culture. ACS Appl Mater Interfaces. 2016;8(28):17885–93.
- [64] Jiang P, Zhang Y, Mu X, Liu D, Liu Y, Guo R, et al. Grayscale stereolithography of gradient hydrogel with site-selective shape deformation. Adv Mater Technol. 2022;7(7):2101288.